Optimizing Mixture Properties for Accurate Laminar Flame Speed Measurement from Spherically Expanding Flame: Application to $H_2/O_2/N_2$/He Mixtures

Y. Zhang[1,2], M. Jeanson[3], R. Mével[1,2], Z. Chen[4] and N. Chaumeix[3]

[1]Center for Combustion Energy, Tsinghua University, Beijing, China
[2]School of Vehicle and Mobility, Tsinghua University, Beijing, China
[3]Institut de Combustion, Aérothermique, Réactivité et Environnement, CNRS-ICARE, France
[4]SKLTCS, CAPT, Department of Mechanics and Engineering Science, College of Engineering, Peking University, Beijing 100871, China
mevel@mail.tsinghua.edu.cn

ABSTRACT

The uncertainty on the laminar flame speed extracted from spherically expanding flames can be minimized by using large flame radius data for the extrapolation to zero stretch-rate. However, at large radii, the hydrodynamic and thermo-diffusive instabilities induce the formation of a complex cellular flame front and limit the range of usable data. In the present study, we have employed the flame stability theory of Matalon to optimize the properties of the initial mixture so that transition to cellularity may occur at a pre-determined, large radius. This approach was employed to measure the laminar flame speeds of $H_2/O_2/N_2$/He mixtures with equivalence ratios from 0.6 to 2.0, at pressures of 50/80/100 kPa and a temperature of 300 K. For all the performed experiments, the uncertainty related to the extrapolation to zero stretch-rate (performed with the linear curvature model) was below 2% as shown by the position of the data points in the ($L_b/R_{f,U}$, $L_b/R_{f,L}$) plan, where L_b is the burned Markstein length; and $R_{f,L}$ and $R_{f,U}$ are the flame radii at the lower and upper bounds of the extrapolation range. Comparison of the predictions of four chemical mechanisms with the present unstretched laminar flame speed data indicated an error below 10% for most conditions. In addition, unsteady 1-D simulations performed with A-SURF demonstrated that the flame dynamical response to stretch rate could not be captured by the mechanisms. The present work indicates that although the stability theory of Matalon provides a well defined framework to optimize the mixture properties for improved flame speed measurement, the uncertainty of some of the required parameters can result in largely over-estimated critical radius for cellularity onset which compromise the accuracy of the optimization procedure.

1. INTRODUCTION

One of the most important fundamental quantity in combustion science is the unstretched laminar flame speed, S_u^0, [1–3]. It is defined as the normal propagation velocity of fresh gas relative to a fixed, planar flame front and represents a measure of the mixture reactivity and diffusivity [1]. Because the turbulent combustion properties scale with the laminar ones [4, 5], accurate experimental data obtained under laminar conditions are needed to predict and model turbulent combustion which is relevant to the conditions found in real applications, such as internal combustion engine or gas turbines [4], or accidental explosion [5, 6]. Laminar flame speed is also widely used to develop and validate detailed reaction models [7, 8] which can then be directly employed within engineering correlations [9] or be reduced/tabulated and included in multi-dimensional numerical simulations [4, 10] with the goal of predicting the risk of accidental combustion events [10, 11], evaluating existing facility [12, 13] or developing and optimizing new combustion devices [14, 15].

Whereas several approaches can be employed to measure the flame speed, including counter flow burners [16], heat flux burners [17, 18], Bunsen burners [19], the spherically expanding flame (SEF) technique is the most widely employed and enables accessing high pressure relevant to real applications [2]. Using the SEF method along with a high-speed visualization system, the laminar flame speed can be extrapolated to zero-stretch rate from the temporal evolution of the radius of a centrally spark-ignited flame. Despite its apparent simplicity, the measurement of the flame speed using the SEF technique is complicated by a number of considerations as reviewed by Lipatnikov et al. [3]. These include: (i) spark ignition energy effects; (ii) confinement effects; (iii) heat losses through radiation; (iv) product density non-uniformity; (v) compression effects; (vi) flame instabilities; and (vii) stretch effects.

Many of these perturbations can be eliminated or mitigated in a simple manner [1, 3]. Perturbations (i) and (iv) only affect flames of small radii and consequently these can be excluded from the analysis of the $R_f(t)$ curve. Perturbations (ii) and (v) are relevant to large flame radii with respect to the combustion vessel's characteristic length scale and the part of the $R_f(t)$ curve affected by these two perturbations can be readily removed from the analysis [20]. Perturbation (iii) is only relevant to slow flames at very large radius, so that many conditions can be studied without considering this limitation. For near flammability limit or decomposition flames [21], which demonstrate low propagation velocity, empirical correlations [22] are available to estimate the increased uncertainty on the flame speed. Perturbations (vi) and (vii) are by far the most challenging especially when targeting a wide range of pressure for the measurements.

The effect of stretch rate on the flame propagation can be accounted for by using various linear or non-linear extrapolation equations [23] which enable to extract the unstretched laminar flame speed from the experimental data obtained with stretched flame. Nevertheless, Wu et al. [23] have demonstrated that, for conditions where the Lewis number (Le) is away from unity, these equations cannot reproduce the flame dynamics which may lead to significant error in the measured unstretched flame speed. Recent studies by Nativel et al. [24] and Huo et al. [25] have shown that, when using large flame radius data, the uncertainty due to the extrapolation method used can be minimized. In particular, Huo et al. have established an error diagram which depends on the Markstein length (L_b) normalized by the initial ($R_{f,L}$) and final ($R_{f,U}$) flame radius data points used for the extrapolation to zero-stretch rate. However, the use of flame with large radii for measuring the flame speed increases the detrimental impact of perturbation (vi). The flame instability, which results in the formation of a cellular flame, is induced, on the one hand, by the gas expansion across the flame front (hydrodynamic or Darrieus-Landau instability), and on the other hand, by the non-equidiffusion of mass and heat of the deficient reactant (thermo-diffusive instability).

The strategy to mitigate the development of cellular instabilities and the extrapolation-induced error

consists in adding helium to the reactive mixture to limit the expansion through the flame front, limiting hydrodynamic instability, and to increase the effective Lewis number of the mixture, decreasing thermo-diffusive instability and stretch impact on flame propagation. Whereas this approach has been implemented by several groups [2, 26–30], it is noteworthy that it has not been generalized and that no well defined scientific procedure has been proposed to optimize the mixture properties to minimize the uncertainty related to perturbations (vi) and (vii).

The goal of the present study is to develop a well defined scientific procedure to optimize the mixture properties so that flame instability is delayed up to a predefined large flame radius, thus allowing to perform the flame speed measurement over a range of radii for which the uncertainty associated with the extrapolation method is minimized. We have developed such a procedure which relies on Matalon's stability theory and applied it to hydrogen-air mixtures over a range of pressure from 50 to 100 kPa.

2. MATERIALS AND METHODS

2.1. Experimental facility

The experimental facility employed has been previously described in [24, 31]. It is a constant volume spherical bomb with inner diameter of 476 mm. Optical access is allowed by two opposite windows with a diameter of 200 mm. The combustion vessel can sustain a maximum pressure of 20 MPa and can be heated up to 573 K using a thermal heating fluid. The visualization of the flame was obtained using a Z-type schlieren arrangement. The process of flame propagation was recorded using a high-speed camera (PHANTOM V1610), with an acquisition rate of up to 25,000 frames per second. Two tungsten electrodes connected to a high voltage power supply enable to centrally spark-ignite the mixture. The spark energy was on the order of 2 mJ as determined from high voltage and current probes measurement. The spherical vessel is equipped with a Kistler piezo-electric pressure transducer (model 601A) synchronized with the imaging system to ensure that the pressure remains constant during the propagation period employed to extract the flame speed. Prior to an experiment, the combustion chamber was evacuated to a pressure on the order of 1 Pa. The reactive mixtures were prepared using the partial pressure method. After all the gas components of the mixture were introduced, eight fans were turned on for 3 minutes to ensure mixture homogeneity. The gas was then let to settle for 3 minutes before ignition.

We studied $H_2/O_2/N_2/(He)$ mixtures for which the ratio of the diluent mole fraction to the oxygen mole fraction was maintained constant at 3.76. The amount of helium introduced in the diluent fraction was optimized to ensure the stability of the flame as described in the following subsection. The hydrogen mole fraction to oxygen mole fraction ratio was defined by the equivalence ratio which ranged between 0.6 and 2.0. All gases were of high-purity grades and supplied by Air Liquide. The initial temperature was between 293 and 300 K, and the pressures were 50/80/100 kPa.

2.2. Procedure to optimize mixture properties

According to the theory of spherical flame stability of Matalon [32–34], the critical flame radius for the onset of cellular instability (R_c) is given by

$$R_c = Pe_c\delta = \delta\frac{\Omega}{\omega} = \frac{\delta}{\omega}\left(Q_1 + \frac{\beta(Le_{eff}-1)}{\sigma-1}Q_2 + PrQ_3\right), \tag{1}$$

where Pe_c is the critical Peclet number; δ is the flame thickness; ω corresponds to the contribution of the hydrodynamic effects to the flame instability; Ω corresponds to the contribution of thermo-diffusive effect to the flame instability; β is the Zeldovich number; Le_{eff} is the effective Lewis number; σ is the expansion ratio; Pr is the Prandtl number; Q_1, Q_2, and Q_3 are complex terms which depend on the expansion ratio, the spherical harmonic wavenumber (n), and the thermal conductivity (λ), see [33].

The flame thickness was calculated using the temperature gradient definition

$$\delta = \frac{T_{ad} - T_u}{(dT/dx)_{max}}, \tag{2}$$

where T_{ad} is the adiabatic flame temperature; T_u is the unburnt gas temperature; and $(dT/dx)_{max}$ is the maximum temperature gradient in a 1-D planar flame. The Zeldovich number β was defined as

$$\beta = E_a \frac{T_{ad} - T_u}{RT_{ad}^2}, \tag{3}$$

where E_a is the activation energy and R is the perfect gas constant.
The effective Lewis number Le_{eff} was obtain from

$$Le_{eff} = 1 + \frac{(Le_E - 1) + (Le_D - 1)\,\varepsilon}{1 + \varepsilon}; \tag{4}$$

where $\varepsilon = 1 + \beta\,(\Xi - 1)$ with $\Xi = \Phi$ for rich mixtures and $\Xi = 1/\Phi$ for lean mixtures. Φ is the equivalence ratio.
All the required parameters were calculated using the thermo-chemical and transport utilities available in the Cantera package [35].

The optimization procedure consisted of the following steps

- Step 1: Define a target critical radius. We have used R_c^t=10 cm, which corresponds to the optical windows radius.
- Step 2: Calculate the theoretical critical radius R_c^{th} for the mixture of interest.
- Step 3: Compare R_c^{th} to R_c^t.
- Step 4: If $R_c^{th} > R_c^t$, stop the procedure.
- Step 5: Calculate the theoretical critical radius $R_c^{th}(He)$ for a mixture with same equivalence diluted only with He.
- Step 6: If $R_c^{th}(He) > R_c^t$, go to step 7.
- Step 6': If $R_c^{th}(He) < R_c^t$, go to step 11.
- Step 7: Replace part of the nitrogen by helium (considering the initial mixture composition).
- Step 8: Calculate the theoretical $R_c^{th}(mod)$ for the modified mixture.
- Step 9: Compare $R_c^{th}(mod)$ and R_c^t.
- Step 10: If $R_c^{th}(mod) = R_c^t$, stop the procedure.
- Step 10': If $R_c^{th}(mod) \neq R_c^t$, repeat step 7 to 9.

- Step 11: Maintaining the hydrogen to oxygen ratio, increase the dilution. The only diluent is helium.
- Step 12: Calculate the theoretical $R_c^{th}(He/mod)$ for the mixture whose dilution level has been modified.
- Step 13: Compare $R_c^{th}(He/mod)$ and R_c^t.
- Step 14: If $R_c^{th}(He/mod) = R_c^t$, stop the procedure.
- Step 14': If $R_c^{th}(He/mod) \neq R_c^t$, repeat step 11 to 13.

A Matlab routine was developed to apply this procedure. The required Cantera calculations were directly launched from Matlab. The built-in Matlab optimization function "fminsearch", which relies on the Nelder-Mead simplex algorithm, was employed to control the modification of the mixture composition. We finally obtain a mixture of a given equivalence ratio whose R_c^{th} is at least 10 cm, so that the flame speed measurement can be performed for large flame radii. It is noted that for the conditions we used in the present study, the dilution was the same as for hydrogen-air mixtures for all cases, i.e. no additional dilution was required to stabilize the flame. The compositions of the mixtures we studied experimentally are given in Table 1.

Table 1: Composition of the $H_2/O_2/N_2$/He mixtures. The initial conditions, the measured parameters, and some calculated parameters are also given.

Φ	X_{H_2}	X_{O_2}	X_{N_2}	X_{He}	$P_1(kPa)$	T_1 (K)	R_c^{ex} (cm)	R_c^{th} (cm)	S_u^0 (cm/s)	L_b (mm)
0.6	0.201	0.168	0.146	0.485	100	297	7.1	10.00	205	0.66
1.0	0.296	0.148	0.379	0.177	100	295	4.5	10.00	268	1.11
1.2	0.335	0.140	0.412	0.114	100	294	5.2	10.00	297	1.19
1.5	0.387	0.129	0.404	0.080	100	296	6.4	10.03	314	0.91
2.0	0.457	0.114	0.429	0.000	100	295	6.8	10.31	292	0.82
0.6	0.201	0.168	0.286	0.345	80	297	7.0	10.00	164	0.50
0.8	0.252	0.157	0.435	0.156	80	296	5.2	10.08	193	0.61
1.0	0.296	0.148	0.556	0.000	80	295	5.2	10.28	215	0.71
1.2	0.335	0.140	0.525	0.000	80	297	6.3	11.35	252	0.95
1.5	0.387	0.129	0.485	0.000	80	295	6.5	11.77	280	0.70
2.0	0.457	0.114	0.429	0.000	80	296	6.6	13.37	278	0.66
0.6	0.201	0.168	0.506	0.125	50	297	5.60	10.00	115	0.48
0.8	0.252	0.157	0.591	0.000	50	299	7.2	13.01	157	0.38
1.0	0.296	0.148	0.406	0.150	50	298	6.7	22.65	235	1.12
1.2	0.335	0.140	0.525	0.000	50	297	6.7	20.20	246	1.38
1.5	0.387	0.129	0.485	0.000	50	296	6.9	20.92	267	1.09
2.0	0.457	0.114	0.429	0.000	50	296	6.7	23.55	272	1.23

2.3. Data reduction procedure

Figure 1 shows an example of spherical flame propagation that we observed experimentally. The evolution of the flame radius as a function of time is obtained using an in-house Matlab program which detects the flame edge and fits a circle to it, thus allowing to deduce the flame radius. Further details about this laminar flame analysis program can be found in [24, 36]. Figure 2 shows a typical $R_f = f(1/R_f)$ curve we obtained, where R_f is the flame radius. The flame speed was obtained by performing a third order differentiation of (R_f, t) data points. Part of the curve is not linear due to the influence of the initiation

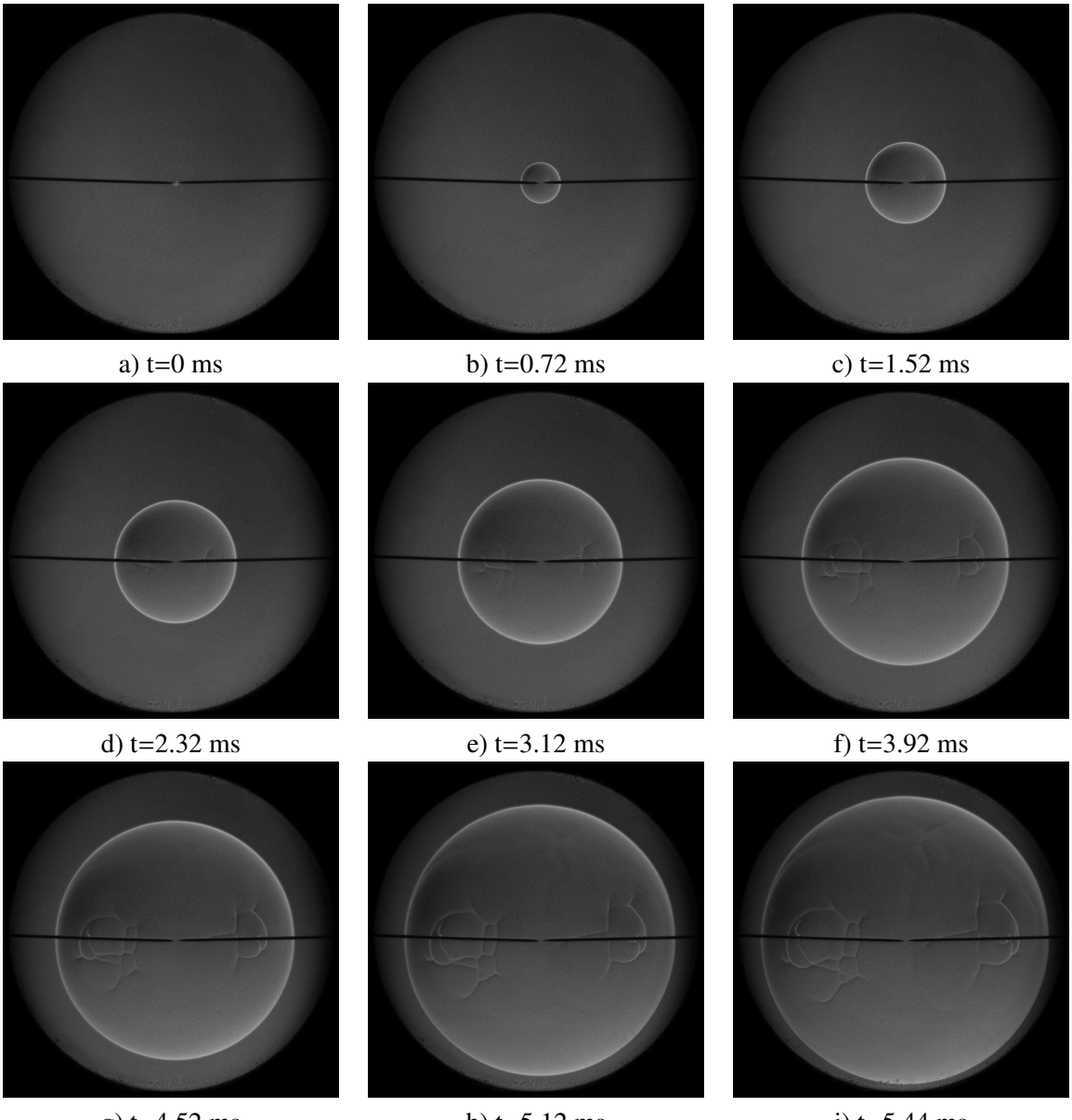

Figure 1: Schlieren images of a spherical flame propagating in a rich hydrogen-air mixture. Conditions: Φ=2; P=82.4 kPa; T=296 K.

energy at low R_f, and of the cellularity onset at high R_f. To select the most appropriate range of data to extract the flame speed, we have employed the two following rules:

- The minimum flame radius ($R_{f,L}$) is simply fixed at 3 cm. This value was selected based on the study of Huo et al. [25].
- The maximum flame radius ($R_{f,U}$) is selected to maximize the linearity of the S_b=f($1/R_f$) in the range [$(1/R_f)_{max}$, $(1/R_f)_{min}$], where $(1/R_f)_{max}$ is obtained using $R_{f,L}$.

This procedure ensured that the data employed for extracting the flame speed, shown as blue crosses in Figure 2, correspond to the phase during which the flame propagates according to the quasi-steady

regime [37].
The unstretched laminar flame speed is extracted using the LC equation [38] which considers a linear relationship between the flame speed and curvature

$$S_b = S_b^0 - 2S_b^0 L_b / R_f \tag{5}$$

where S_b is the stretched flame speed with respect to the burnt gas; S_b^0 is the unstretched flame speed with respect to the burnt gas; and L_b is the Markstein length. The choice of the LC equation was motivated by the results of Chen [39] which showed that for mixtures with positive Markstein length, this equation is the most accurate to extract the flame speed. Figure 2 also shows the evolution of the flame speed as a function of stretched rate calculated with Equation 5 and the parameters S_b^0 and L_b obtained by fitting the experimental data. The laminar flame speed with respect to the unburnt gas, S_u^0, was obtained by dividing S_b^0 by the expansion ratio at chemical equilibrium.

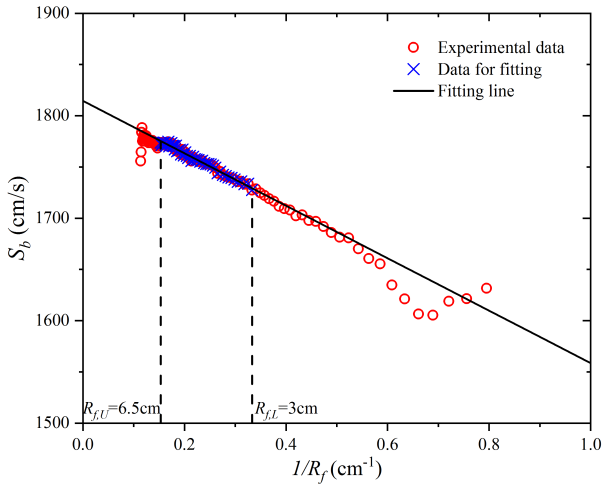

Figure 2: Evolution of the stretched flame speed as a function of $1/R_f$. Conditions: H_2/air mixture; Φ=1.5; X_{He}=0; P=80 kPa; T=300 K.

2.4. Numerical simulations

The steady 1-D freely propagating flame code of the Cantera package [35] was employed to calculate the unstretched laminar flame speed. The multi-component transport model was adopted and the Soret effect was taken into account. As previously mentioned, the Cantera package was also employed to calculate the thermodynamic and transport properties required for the optimization of the mixture's composition. In addition, unsteady expanding spherical flames were simulated using A-SURF, which detailed description can be found in [40, 41]. The initial conditions of velocity and wall temperature at each grip point before ignition were 0 cm/s and 300 K. To avoid perturbation due to confinement effects [42], the radius of the spherical numerical domain was set at r=120 cm. The flame radius used for determining the laminar flame speed and the Markstein length was less than 10 cm, to be consistent with the experiments. The radiation effect was neglected. Multi-component transport and Soret effects were also included in the A-SURF simulations.

For the optimization procedure, the only detailed reaction model used was that of Wang et al. [43] which consists of 14 species and 38 reactions. We have also verified the performances of three other reaction models: Konnov's model [44] (15 species and 75 reactions); Burke's model [45] (13 species and 27 reactions); and Curran's model [46] (11 species and 21 reactions).

3. RESULTS AND DISCUSSION

3.1. Critical flame radius for cellurity onset

As seen in Figure 1, the flame surface remains essentially smooth up to a flame radius of several cm. The initial perturbation induced at the ignition stage by the presence of the electrodes [47] does not grow for several ms. Eventually, because of the decrease of the stabilization by the thermo-diffusive effects at large radii, a cellular structure develops from the initial perturbation and progressively covers the flame surface. The development of the cellular structure is accompanied by oscillations of the apparent flame speed as the cells undergo successive phases of growth and breaking. Because determining the critical radius for cellularity onset through a visual inspection can lead to a subjective interpretation, we have chosen to define it as the last flame radius that we employed in our flame speed analysis. As a consequence, the R_c values that we are reporting correspond to the maximum flame radius for which the flame propagation is not affected by the development of the cellular flame front. These values are reported in Table 1.

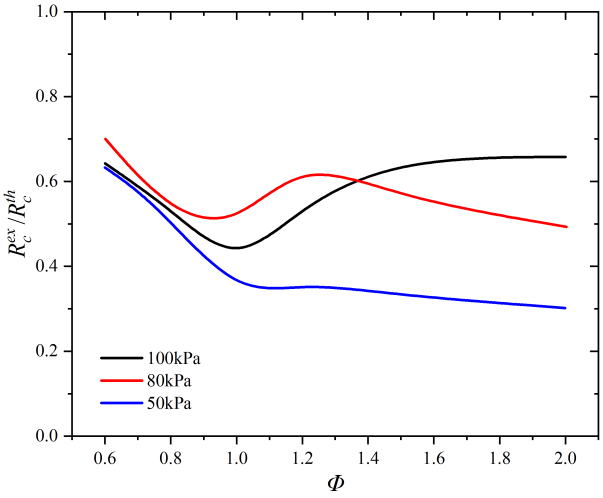

Figure 3: Deviation of R_c from R_c^{th} predicted by Matalon's theory for $H_2/O_2/N_2$/He mixtures at T=300 K.

Figure 3 shows the evolution of the ratio R_c^{ex}/R_c^{th} with equivalence ratio for the three pressures we investigated. This ratio ranges between 0.3 and 0.7, which indicates that the theory of Matalon significantly over-estimate the critical radius for cellularity onset. It is also noted that the deviation is lower at 80/100 kPa as compared to the one observed at 50 kPa. Although under certain conditions, the theory of Matalon predicts with good accuracy the critical radius (or Peclet number) for cellularity onset, discrepancies of up to factor of 4 between the predicted and measured critical radius were previously reported by Law et al. [48]. It should be noted that some of the parameters, such as the Zeldovich number, that need to be calculated to determine R_c^{th} may exhibit large uncertainty. Grosseuvres et al. [49] have recently demonstrated the inability of several detailed reaction models to reproduce the experimentally measured activation energy which directly impact the value of the Zeldovich number and thus the predicted impact of the thermo-diffusive effect, see Equation 1 and Equation 3.

3.2. Flame speed measurements

Figure 4 shows the position of the experimental data points in the diagram of extrapolation-induced uncertainty established by Huo et al. [25]. The uncertainty related to the extrapolation to zero stretch-

rate is below 2% for all the experimental cases performed in this study which reveals the relevance of the mixture properties optimization and data reduction procedures we applied. The overall uncertainty on the flame speed measured (ΔS_u^0) can be estimated using the formula employed by Nativel et al. [24]

$$\Delta S_u^0 = \sqrt{(\Delta S_{u,ext})^2 + (\Delta S_{u,T})^2 + \left(\Delta S_{u,rf}\right)^2 + (\Delta S_{u,rad})^2} \tag{6}$$

where $\Delta S_{u,ext}$ is the uncertainty due to the extrapolation to zero stretch rate, taken equal to 2%; $\Delta S_{u,T}$ is the uncertainty due to the uncertainty on the temperature, taken equal to 0.4%; $\Delta S_{u,rf}$ is the uncertainty due to the uncertainty on the flame radii, taken equal to 0.9%; and $\Delta S_{u,rad}$ is the uncertainty due to radiation, taken equal to 0.7%. This analysis leads to a maximum uncertainty of 2.3%.

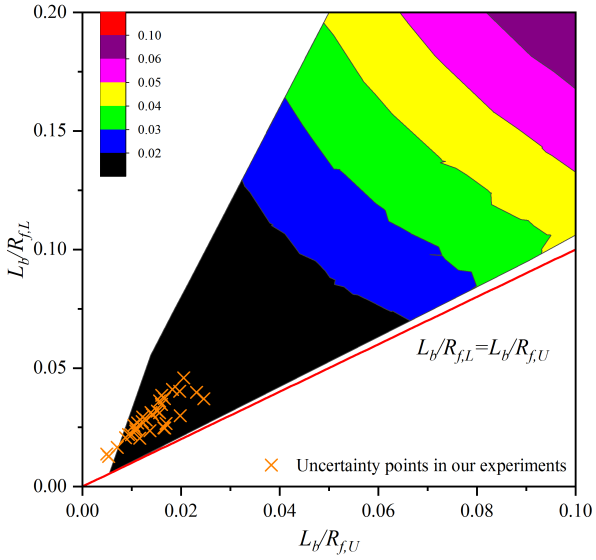

Figure 4: Experimental data points in the map of extrapolation uncertainty. Conditions: $H_2/O_2/N_2$/He mixtures; Φ=0.6-2; P=50-100 kPa; T=293-300 K.

Figure 5 shows the evolution of the flame speed as a function of equivalence ratio for the three pressures investigated. For all pressures, the flame speed increases in the range Φ=0.6 to Φ=1.5. In the range Φ=1.5 to Φ=2.0, the flame speed plateaus at P=50 and 80 kPa and decreases at P=100 kPa. Similar trends were observed in previous studies [26, 50, 51] and are explained by the respective changes of the mixture diffusivity and of the chemical energy release rate with equivalence ratio. Under the conditions we have studied, the flame speed is increasing with pressure for all equivalence ratio. Although the interpretation of the results is complicated by the simultaneous change of the flame temperature and the pressure, it might be concluded that under the conditions we employed, both the chain terminating reaction $H+O_2+M=HO_2+M$ and the chain branching reaction $H+O_2=OH+O$ promote flame propagation. It was shown by Yang et al. [52] using sensitivity analysis, that the competition between these two chemical paths is a complex function of temperature, pressure and mixture's initial composition.

3.3. Chemical model predictions

Figure 5 compares the experimental laminar flame speed with the prediction of the four reaction models we have selected. The performances of the mechanisms were quantified and the deviation between the

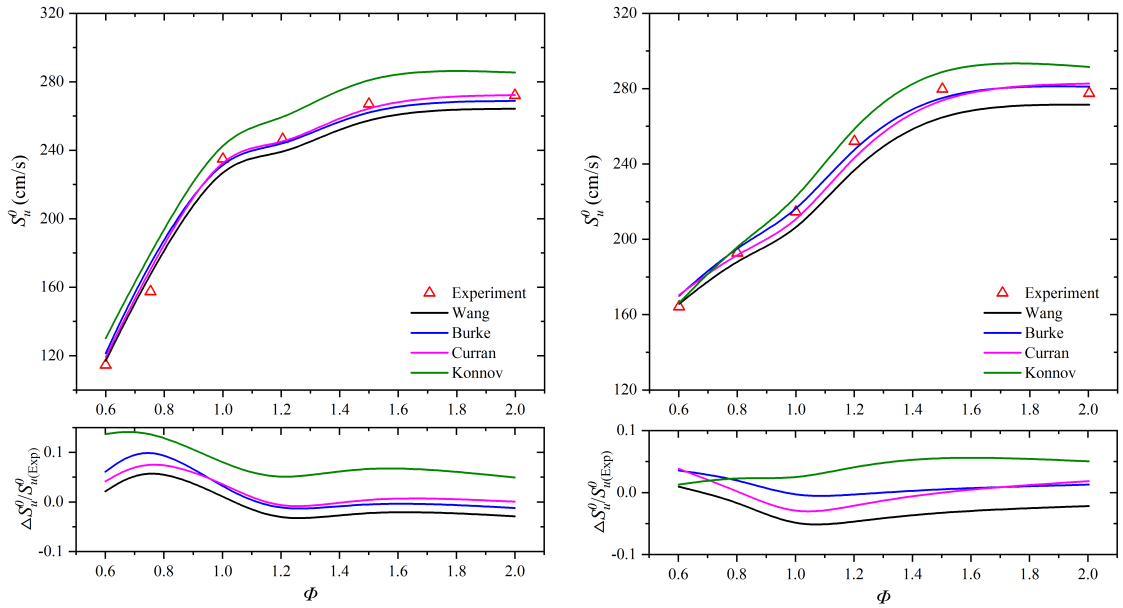

a) P = 50 kPa

b) P = 80 kPa

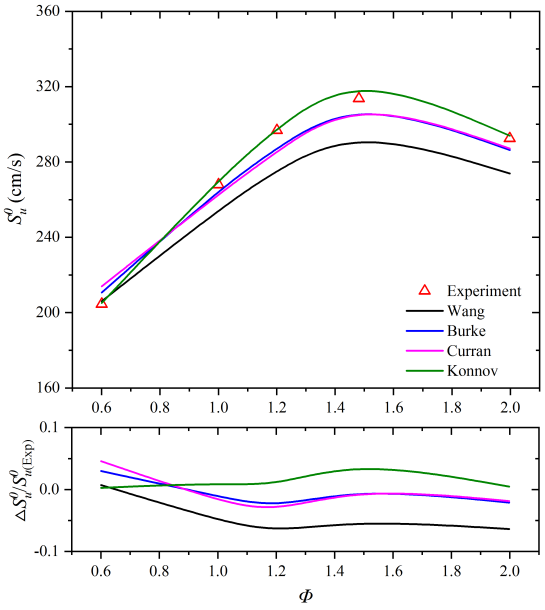

(c) P = 100 kPa

Figure 5: Comparison between the experimental and calculated unstretched laminar flame speed for $H_2/O_2/N_2$/He mixtures at different pressures and T=293-300 K.

experimental and calculated values are also shown in Figure 5. The relative error on S_u^0 ($E_r\left(S_u^0\right)$) was calculated using

$$E_r\left(S_u^0\right) = \frac{\Delta S_u^0}{S_{u(Exp)}^0} = \frac{S_{u(Cal)}^0 - S_{u(Exp)}^0}{S_{u(Exp)}^0}, \tag{7}$$

where $S_{u(Exp)}^0$ and $S_{u(Cal)}^0$ are the experimental and calculated unstretched laminar speed, respectively. For these calculations, the freely propagating flame code in Cantera was employed. All four models reproduce qualitatively the trends observed experimentally. Quantitatively, the deviation between the

experiments and the different models is below 10% except for Konnov's model in the case for which Φ=0.6 and P=50 kPa. It is noted that the model of Konnov tends to over-estimate the flame speed in general whereas the model of Wang tends to under-estimate it. The results obtained with Burke's and Curran's models are close and agree better with the experimental data than the results obtained with Konnov's and Wang's models. The Curran's model performs better at 50 kPa, whereas the Burke's model performs better at 80 kPa and 100 kPa. The mean absolute error for the models of Burke, Curran, Konnov, and Wang are, 2.6%, 2.7%, 4.9%, 3.6%, respectively.

We have also evaluated the ability of the reaction models to reproduce the dynamical response of the flame to stretch rate using unsteady simulation performed with A-SURF. An example of such a calculation is shown in Figure 6. For the case presented, the behavior observed experimentally is qualitatively and quantitatively captured by the reaction model.

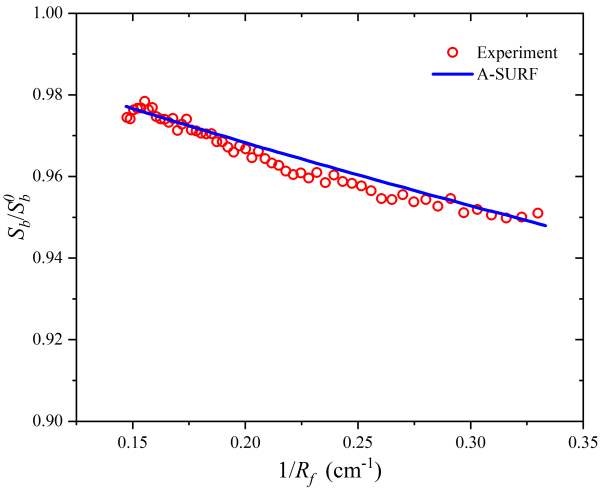

Figure 6: Experimental and simulated non-dimensional stretched flame speeds as a function of $1/R_f$. Conditions: Φ=2; X_{He}=0; P=100 kPa; T=300 K. The simulation was performed with Wang's model.

As the dynamical response of the flame to stretch rate is quantified by the Markstein length, we have compared the experimental and calculated values obtained for this parameter, as shown in Figure 7. Qualitatively, the models tend to better reproduce the evolution of the Markstein length with equivalence ratio at P=50 kPa. At higher pressures, the models essentially fail at reproducing the U-shaped curves observed experimentally with a maximum at Φ=1.2. It is also noted that Curran's and Burke's models predict a negative Markstein length in the case for which Φ=0.6 and P=50 kPa, whereas a positive Markstein length was measured. This indicates that these two models predict an increase of the flame speed with the increase of stretch rate whereas a decrease is observed experimentally. Quantitatively, the mean absolute error on the Markstein length, calculated in the same way as the error on the flame speed, see Equation 7, for the models of Burke, Curran, Konnov, and Wang are, 31.4%, 44.6%, 26.8%, 27.3%, respectively.

4. CONCLUSION

In the present study, a numerical implementation of the stability theory of Matalon has been employed to optimize the mixture properties so that the development of the cellular flame front is delayed up to a predefined flame radius. Using the large flame radius data, the unstretched laminar flame speed was measured in the quasi-steady regime, in which the uncertainty associated with the extrapolation method

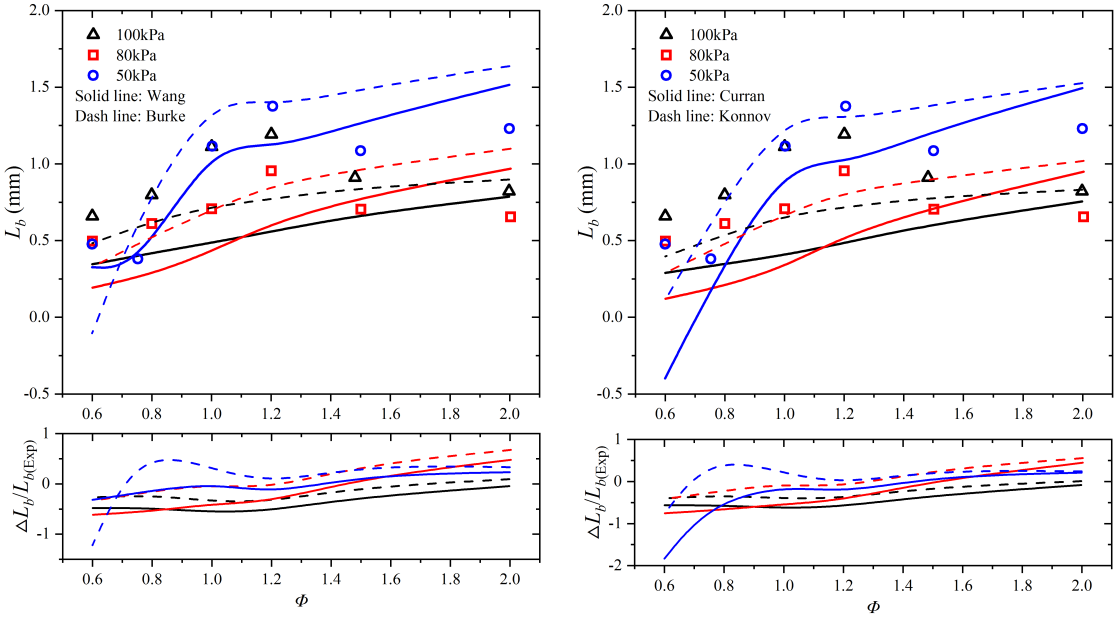

Figure 7: Comparison between the experimental and calculated Markstein length for $H_2/O_2/N_2$/He mixtures at T=293-300 K and P=50/80/100 kPa.

is minimum. Although the experimental critical radius was found to be significantly lower than the theoretical one, the flame speeds measured exhibit an uncertainty below 2.3%. The performances of four models from the literature were evaluated with respect to the unstretched laminar flame speed and the Markstein length using steady and unsteady numerical simulation performed with the multi-component transport model and the Soret diffusion. While the flame speed was reproduced within 5% on average by the four models, large discrepancies, above 25% on average, were observed for the Markstein length.

ACKNOWLEDGMENTS

The present study was founded by the Programme Investissement d'Avenir-MITHYGENE grant agreement no. ANR-11-RSNR-0015 and by the Natural Science Foundation of China under grant number 51750110502. RM was also supported by a start-up fund of the Center for Combustion Energy of Tsinghua University and the 1000 Young Talents of China program. RM is grateful to the French Labex CAPRYSSES program, grant agreement no. ANR-11-LABX-0006-01, for supporting his visit at ICARE-CNRS Orléans as a visiting professor.

REFERENCES

1. F. Egolfopoulos, N. Hansen, Y. Ju, K. Kohse-Hoinghaus, C. Law, F. Qi, Advances and challenges in laminar flame experiments and implications for combustion chemistry, Progress in Energy and Combustion Science 43 (2014) 36–67.
2. C. Xiouris, T. Ye, J. Jayachandran, F. Egolfopoulos, Laminar flame speeds under engine-relevant conditions: Uncertainty quantification and minimization in spherically expanding flame experiments, Combustion and Flame 163 (2016) 270 – 283.
3. A. Lipatnikov, S. Shy, W. Li, Experimental assessment of various methods of determination of laminar flame speed in experiments with expanding spherical flames with positive markstein lengths, Combustion and Flame 162 (7) (2015) 2840 – 2854.

4. S. Lapointe, G. Blanquart, Fuel and chemistry effects in high karlovitz premixed turbulent flames, Combustion and Flame 167 (2016) 294 – 307.
5. L. Boeck, S. Lapointe, J. Melguizo-Gavilanes, G. Ciccarelli, Flame propagation across an obstacle: OH-PLIF and 2-D simulations with detailed chemistry, Proceedings of the Combustion Institute 36 (2) (2017) 2799–2806.
6. L. Boeck, M. Kellenberger, G. Rainsford, G. Ciccarelli, Simultaneous OH-PLIF and schlieren imaging of flame acceleration in an obstacle-laden channel, Proceedings of the Combustion Institute 36 (2) (2017) 2807 – 2814.
7. G. Blanquart, P. Pepiot-Desjardins, H. Pitsch, Chemical mechanism for high temperature combustion of engine relevant fuels with emphasis on soot precursors, Combustion and Flame 156 (2009) 588–607.
8. O. Park, P. Veloo, D. Sheen, Y. Tao, F. Egolfopoulos, H. Wang, Chemical kinetic model uncertainty minimization through laminar flame speed measurements, Combustion and Flame 172 (2016) 136 – 152.
9. R. Mével, F. Lafosse, L. Catoire, N. Chaumeix, G. Dupré, C. E. Paillard, Induction delay times and detonation cell size prediction of hydrogen-nitrous oxide-argon mixtures, Combustion Science and Technology 180 (2008) 1858–1875.
10. R. Mével, D. Davidenko, F. Lafosse, N. Chaumeix, G. Dupré, C. E. Paillard, J. E. Shepherd, Detonation in hydrogen-nitrous oxide-diluent mixtures: an experimental and numerical study, Combustion and Flame 162 (2015) 1638–1649.
11. J. Goulier, A. Comandini, F. Halter, N. Chaumeix, Experimental study on turbulent expanding flames of lean hydrogen/air mixtures, Proceedings of the Combustion Institute 36 (2) (2017) 2823–2832.
12. K. Grogan, M. Ihme, Regimes describing shock boundary layer interaction and ignition in shock tubes, Proceedings of the Combustion Institute 36 (2) (2017) 2927 – 2935.
13. M. Ihme, On the role of turbulence and compositional fluctuations in rapid compression machines: Autoignition of syngas mixtures, Combustion and Flame 159 (4) (2012) 1592 – 1604.
14. Z. Wang, F. Li, Y. Wang, A generalized kinetic model with variable octane number for engine knock prediction, Fuel 188 (2017) 489 – 499.
15. L. Magri, Y.-C. See, O. Tammisola, M. Ihme, M. Juniper, Multiple-scale thermo-acoustic stability analysis of a coaxial jet combustor, Proceedings of the Combustion Institute 36 (3) (2017) 3863 – 3871.
16. C. Ji, E. Dames, Y. Wang, H. Wang, F. Egolfopoulos, Propagation and extinction of premixed C_5-C_{12} n-alkane flames, Combustion and Flame 157 (2010) 277–287.
17. M. Christensen, A. Konnov, Laminar burning velocity of diacetyl + air flames. further assessment of combustion chemistry of ketene, Combustion and Flame 178 (2017) 97 – 110.
18. E. Nilsson, A. van Sprang, J. Larfeldt, A. Konnov, The comparative and combined effects of hydrogen addition on the laminar burning velocities of methane and its blends with ethane and propane, Fuel 189 (2017) 369 – 376.
19. R. Shang, Y. Zhang, M. Zhu, Z. Zhang, D. Zhang, G. Li, Laminar flame speed of CO_2 and N_2 diluted H_2/CO/air flames, International Journal of Hydrogen Energy 41 (33) (2016) 15056 – 15067.
20. J. Beeckmann, R. Hesse, J. Schaback, H. Pitsch, E. Varea, N. Chaumeix, Flame propagation speed and markstein length of spherically expanding flames: Assessment of extrapolation and measurement technique, Proceedings of the Combustion Institute 37 (2) (2019) 1521–1528.
21. S. Jerzembeck, M. Matalon, N. Peters, Experimental investigation of very rich laminar spherical flames under microgravity conditions, Proceedings of the Combustion Institute 32 (2009) 1125–1132.
22. H. Yu, W. Han, J. Santner, X. Gou, C. Sohn, Y. Ju, Z. Chen, Radiation-induced uncertainty in laminar flame speed measured from propagating spherical flames, Combustion and Flame 161 (2014) 2815–2824.
23. F. Wu, W. Liang, Z. Chen, Y. Ju, C. Law, Uncertainty in stretch extrapolation of laminar flame speed from expanding spherical flames, Proceedings of the Combustion Institute 35 (0) (2015) 663–670.
24. D. Nativel, M. Pelucchi, A. Frassoldati, A. Comandini, A. Cuoci, E. Ranzi, N. Chaumeix, T. Faravelli, Laminar flame speeds of pentanol isomers: An experimental and modeling study, Combustion and Flame 166 (2016) 1 – 18.
25. J. Huo, S. Yang, Z. Ren, D. Zhu, C. K. Law, Uncertainty reduction in laminar flame speed extrapolation for expanding spherical flames, Combustion and Flame 189 (2018) 155–162.
26. S. Tse, D. Zhu, C. Law, Morphology and burning rates of expanding spherical flames in H_2/O_2/inert mixtures up to 60 atmospheres, Proceedings of the Combustion Institute 28 (2) (2000) 1793 – 1800.
27. X. Shen, X. Yang, J. Santner, J. Sun, Y. Ju, Experimental and kinetic studies of acetylene flames at elevated pressures, Proceedings of the Combustion Institute 35 (1) (2015) 721 – 728.
28. W. Zhang, X. Gou, W. Kong, Z. Chen, Laminar flame speeds of lean high-hydrogen syngas at normal and elevated pressures, Fuel 181 (2016) 958 – 963.
29. M. Han, Y. Ai, Z. Chen, W. Kong, Laminar flame speeds of H_2/CO with CO_2 dilution at normal and elevated pressures and temperatures, Fuel 148 (2016) 32–38.
30. Y. Ai, Z. Zhou, Z. Chen, W. Kong, Laminar flame speed and markstein length of syngas at normal and elevated pressures and temperatures, Fuel 137 (2014) 339–345.
31. J. Goulier, N. Chaumeix, F. Halter, N. Meynet, A. Bentab, Experimental study of laminar and turbulent flame speed of a spherical flame in a fan-stirred closed vessel for hydrogen safety application, Nuclear Engineering and Design 312 (2017) 214–227.
32. M. Matalon, B. Matkowsky, Flames as gasdynamic discontinuities, Journal of Fluid Mechanics 124 (1982) 239–259.
33. R. Addabbo, J. K. Bechtold, M. Matalon, Wrinkling of spherically expanding flames, Proceedings of the Combustion Institute 29 (2002) 1527–1535.

34. M. Matalon, Flame dynamics, Proceedings of the Combustion Institute 32 (2009) 57–82.
35. D. G. Goodwin, R. L. Speth, H. K. Moffat, B. W. Weber, Cantera: An object-oriented software toolkit for chemical kinetics, thermodynamics, and transport processes, https://www.cantera.org, version 2.4.0 (2018).
36. R. Mével, F. Lafosse, N. Chaumeix, G. Dupré, C.-E. Paillard, Spherical expanding flames in H_2-N_2O-Ar mixtures: Flame speed measurement and kinetic modeling., International Journal of Hydrogen Energy 34 (21) (2009) 9007–9018.
37. A. Kelley, C. Law, Nonlinear effects in the extraction of laminar flame speeds from expanding spherical flames, Combustion and Flame 156 (2009) 1844–1851.
38. M. Frankel, G. Sivashinsky, On effects due to thermal expansion and lewis number in spherical flame propagation, Combustion Science and Technology 31 (1983) 131–138.
39. Z. Chen, On the extraction of laminar flame speed and markstein length from outwardly propagating spherical flames, Combustion and Flame 158 (2) (2011) 291–300.
40. Z. Chen, On the accuracy of laminar flame speeds measured from outwardly propagating spherical flames: Methane/air at normal temperature and pressure, Combustion and Flame 162 (6) (2015) 2442–2453.
41. Z. Chen, Effects of radiation and compression on propagating spherical flames of methane/air mixtures near the lean flammability limit, Combustion and Flame 157 (12) (2010) 2267–2276.
42. M. P. Burke, Z. Chen, Y. Ju, F. L. Dryer, Effect of cylindrical confinement on the determination of laminar flame speeds using outwardly propagating flames, Combustion and Flame 156 (4) (2009) 771–779.
43. S. G. Davis, A. V. Joshi, H. Wang, F. Egolfopoulos, An optimized kinetic model of H_2/CO combustion, Proceedings of the Combustion Institute 30 (1) (2005) 1283–1292.
44. A. A. Konnov, Yet another kinetic mechanism for hydrogen combustion, Combustion and Flame 203 (2019) 14 – 22.
45. M. P. Burke, M. Chaos, Y. Ju, F. L. Dryer, S. J. Klippenstein, Comprehensive H_2/O_2 kinetic model for high-pressure combustion, International Journal of Chemical Kinetics 44 (7) (2011) 444–474.
46. M. Ó. Conaire, H. J. Curran, J. M. Simmie, W. J. Pitz, C. K. Westbrook, A comprehensive modeling study of hydrogen oxidation, International Journal of Chemical Kinetics 36 (11) (2004) 603–622.
47. S. Bane, J. Ziegler, J. Shepherd, Investigation of the effect of electrode geometry on spark ignition, Combustion and Flame 162 (2) (2015) 462 – 469.
48. C. Law, G. Jomaas, J. Bechtold, Cellular instabilities of expanding hydrogen/propane spherical flames at elevated pressures: theory and experiment, Proceedings of the Combustion Institute 30 (2005) 159–167.
49. R. Grosseuvres, A. Comandini, A. Bentaib, N. Chaumeix, Combustion properties of H_2/N_2/O_2/steam mixtures, Proceedings of the Combustion Institute 37 (2) (2019) 1537–1546.
50. W. Kim, Y. Sato, T. Johzaki, T. Endo, D. Shimokuri, A. Miyoshi, Experimental study on self-acceleration in expanding spherical hydrogen-air flames, International Journal of Hydrogen Energy 43 (27) (2018) 12556 – 12564.
51. Q. Liu, X. Chen, Y. Shen, Y. Zhang, Parameter extraction from spherically expanding flames propagated in hydrogen/air mixtures, International Journal of Hydrogen Energy 44 (2) (2019) 1227 – 1238.
52. S. Yang, X. Yang, F. Wu, Y. Ju, C. Law, Laminar flame speeds and kinetic modeling of H_2/O_2/diluent mixtures at subatmospheric and elevated pressures, Proceedings of the Combustion Institute 36 (1) (2017) 491–498.